DOI: 10.61782/fa.2023.0287

forum acusticum 2023

THREE-DIMENSIONAL GRIDLESS IMAGING OF AEROACOUSTICAL FIELDS WITH SONONS BASED ON A HIERARCHICAL BAYESIAN FRAMEWORK

Zijian NIU[1*] **Jérôme Antoni**[1] **Simon Bouley**[2]

[1] Univ Lyon, INSA Lyon, LVA, EA677, 69621 Villeurbanne, France
[2] MicrodB, 28 Chemin du Petit Bois, Écully Cedex, F-69134, France

ABSTRACT

The imaging of aeroacoustic fields by means of microphone arrays is a complex task due to the 3D nature of volumetric sources in turbulent flow. Rather than meshing the full space for the identification of aeroacoustical source distributions, the aim of this work is to reconstruct the acoustic sound fields generated by an equivalent set of point sources with free coordinates, called "acoustic sonons". Their radiation is expected to reproduce the same acoustical properties as the measured acoustical field, such as its pressure level, its directivity, and its spatial coherence by retrieving phase information. It is shown that the proposed concept of sonons, while being very flexible, effectively provides equivalent representations for a large variety of source distributions, whether they are initially composed of monopoles, dipoles, or quadrupoles, and whether these are spatially coherent or not. Additionally, source position priors can be taken into account in sonons generation, which improves localization ability. The problem is solved within a probabilistic framework, by means of a hierarchical Bayesian model inferred witha dedicated Markov chain Monte Carlo algorithm. The performance of the method is evaluated on two analytical test cases composed of the radiation of elementary sources and of a trailing edge.

*__Corresponding author__: *zijian.niu@insa-lyon.fr.*

Keywords: *Source identification, Gridless method, Equivalent source method, Markov chain Monte Carlo*

1. INTRODUCTION

Acoustic source reconstruction has played a significant role in the aeroacoustic domain throughout the last several years. The measurement of aerodynamic noise presents additional challenges, such as more complicated physical phenomena involved and large studied objects in wind tunnels, all of which limit the usage of standard methods. Most approaches, like conventional beamforming (CBF), assume that potential sources are located at a finite collection of candidate points, which are used to estimate the source intensity [1]. A well-known issue with this is the basis mismatch, which occurs when the grid does not represent the real position of the sources; this can cause severe mistakes in real applications. Moreover, in 3D, the number of grid points increases dramatically, sometimes making the computation time of grid-based methods unacceptable.

To address these limitations, alternative methods, like gridless localization algorithms, have been proposed. Xenaki et al. [2] developed an 1D gridless compressive beamforming based on the sparsity hypothesis, which was then validated in 2D [3]. Chardon et al. [4] recently proposed a three-dimensional gridless method by solving a Beurling LASSO problem. However, these methods have the limitation that the sparse condition cannot always be satisfied. As a traditional optimization method, the idea of applying global optimization to sound source localization has also been exploited in recent years. Malgoezar

et al. [5] demonstrated the Differential Evolution method, which can reliably identify incoherent sources. Later, Wei et al. [6] extended this method to 3D with a Partial Swarm Optimization algorithm. Some new papers have been published that provide alternative optimization strategies, such as the state transition algorithm in reverberant environments [7] or the signal subspace approach [8]. The fundamental shortcoming of these techniques is that they did not address the identification of correlated sources. In addition, with the development of AI, machine learning techniques are being applied to gridless sound source localization problems [9–11]. These methods inevitably suffer from an enormous training phase, which hinders their immediate use.

This contribution presents a novel solution. Instead of performing full-space meshing for the identification of aeroacoustic sources, the aim is to reconstruct the acoustic sound field generated by an equivalent set of point sources with free coordinates, which are not located on any predefined grid. Their radiation is expected to reproduce the same acoustic properties as the measured acoustic field. The statistical equivalence concept proposed for these sources is very flexible and can be effectively used to provide the equivalent representations for a diverse range of source distributions, whether they are initially composed of monopoles, dipoles, or quadrupoles, and with or without spatial coherence.

Moreover, in spite of the various approaches that have been proposed in the literature, the reconstruction of the directivity of sound fields has rarely been studied directly, which requires a correct estimation of the source phase as well as the mutual correlation of the sources. As far as we know, there has been few attempts to address these issues [12], which our equivalent source model will be shown to easily handle.

In what follows, the new gridless source localization model is presented together with its algorithm based on the Bayesian framework. First, a Bayesian probabilistic model is developed [13, 14], and then a Markov chain Monte Carlo (MCMC) sampler of the posterior probability density function (PDF) is introduced. Finally, the application is demonstrated on simulated data.

2. PROBABILISTIC MODEL

2.1 "Sonon" definition

The objective is to represent the acoustic field by sets of acoustic monopoles, hereafter referred to as "sonons". The name "sonon" is inspired by an analogy with the particles found in an atom such as a proton to represent the unit particle of sound. The sonons are allowed to explore freely the 3D space and are not constrained to any predefined grid. Each sonon is fundamentally characterized by its position and its amplitude.

2.2 Radiation equation

Suppose that the acoustic signal radiated by N sonons is received by an array containing M microphones, and the signal is cut into I snapshots. After short-time Fourier transforms, let p_{mi} denote the Fourier coefficient at the m-th microphone in the i-th snapshot. Let q_{ni} be the amplitude of the n-th sonon, located at $\mathbf{r}_n = (x_n, y_n, z_n)$. The observed pressures are related to the sonon amplitudes as

$$p_{mi} = \sum_{n=1}^{N} G_m(\mathbf{r}_n) q_{ni} + \nu_{mi}, \tag{1}$$

where $G_m(\mathbf{r}_n)$ is the Green function between point $\mathbf{r}_n$ and the m-th microphone position, denoted by $\mathbf{r}_m$, and ν_{mi} stands for an additive error. In free field conditions, at the given frequency f, $G_m(\mathbf{r}_n)$ is given by

$$G_m(\mathbf{r}_n) = \frac{\exp(-ik\|\mathbf{r}_n - \mathbf{r}_m\|)}{4\pi\|\mathbf{r}_n - \mathbf{r}_m\|}, \tag{2}$$

where $k = 2\pi f/c$ and c is the sound speed. In matrix form, the relationship reads

$$\mathbf{P} = \mathbf{G}(\mathbf{r})\mathbf{Q} + \mathbf{N}, \tag{3}$$

where, $\mathbf{P} = [\mathbf{p}_1, ..., \mathbf{p}_I]^T \in \mathbb{C}^{M\times I}$, $\mathbf{r} = [\mathbf{r}_1^T, ..., \mathbf{r}_N^T]^T \in \mathbb{R}^{3N}$, $\mathbf{Q} = [\mathbf{q}_1, ..., \mathbf{q}_I]^T \in \mathbb{C}^{N\times I}$ and $\mathbf{N} = [\mathbf{n}_1, ..., \mathbf{n}_I]^T \in \mathbb{C}^{M\times I}$.

The objective is to infer the positions $\mathbf{r}_n$ and the complex-valued amplitudes q_{ni} of the N sonons from the observations p_{mi}.

2.3 Hierarchical model

The two unknowns $\mathbf{Q}$ and $\mathbf{r}$ are regarded as random variables in a Bayesian formulation. The objective is to find their posterior distribution $[\mathbf{r}, \mathbf{Q}|\mathbf{P}]$. These variables are integrated into a Bayesian hierarchical model. According to Bayes' Theorem,

$$[\mathbf{r}, \mathbf{Q}|\mathbf{P}] = \prod_{i=1}^{I} \frac{[\mathbf{p}_i|\mathbf{r}, \mathbf{q}_i][\mathbf{q}_i|\mathbf{r}]}{[\mathbf{p}_i]}[\mathbf{r}]. \tag{4}$$

2.3.1 Likelihood function

The radiation function indicates that the observed data in each snapshot, represented by $\mathbf{p}_i$, obey the same PDF as of the additive error, which can reasonably be approximated as a complex Gaussian with mean $\mathbf{G}(\mathbf{r})\mathbf{q}_i$ and covariance matrix $\mathbf{\Sigma}_n = diag(\sigma_0^2)$,

$$[\mathbf{p}_i|\text{rest}] \propto \mathcal{CN}(\mathbf{p}_i; \mathbf{G}(\mathbf{r})\mathbf{q}_i, \mathbf{\Sigma}_n). \tag{5}$$

where "|rest" means conditioned to all other variables.

2.3.2 Priors

The prior PDF reflects the user's expectation or knowledge before the measurements. In our model, different from the grid-based approach that assumes that the source position has equal probability over a predefined and limited grid, we give a prior PDF to the positions of the sonons and infer their posterior PDF. A possible prior would be the Gaussian distribution centered on the prior acoustic center of the source distribution. For simplicity, and without loss of generality, let's place the latter at the frame origin, so that,

$$[\mathbf{r}] \propto \mathcal{N}(\mathbf{r}; 0, \lambda^2\mathbf{I}), \tag{6}$$

where λ^2 controls the variance of sonons position.

For the source amplitudes, as the Fourier coefficients are not known in advance, the zero mean complex Gaussian distribution is chosen,

$$[\mathbf{q}_i|\mathbf{r}] \propto \mathcal{CN}(\mathbf{q}_i; 0, \gamma^2\mathbf{\Sigma}_q), \tag{7}$$

where $[\mathbf{\Sigma}_q]_{ij}$ is the covariance matrix that describes the spatial coherence between two sonons located at $\mathbf{r}_i$ and $\mathbf{r}_j$, and γ^2 controls the prior absolute amplitude.

2.3.3 Hyperpriors

In the previous analysis, three hyperparameters were added to control the variance of position, the noise and the source powers. These hyperparameters are also allocated an PDF for later inference. The inverse Gamma law is chosen for its simplicity:

$$[\gamma^2] \propto \mathcal{IG}(a_\gamma, b_\gamma), \tag{8}$$

$$[\lambda^2] \propto \mathcal{IG}(a_\lambda, b_\lambda), \tag{9}$$

and

$$[\sigma_0^2] \propto \mathcal{IG}(a_{\sigma_0}, b_{\sigma_0}). \tag{10}$$

3. MCMC ALGORITHM

Based on the Bayesian formulation presented in the previous section, the objective is to sample from the posterior PDF $[\mathbf{q}_i, \mathbf{r}, \gamma^2, \sigma_0^2, \lambda^2|\mathbf{p}_i]$, for which no form is known. The Gibbs sampler is appropriate for this scenario.

3.1 Collapsed Gibbs sampler

The Gibbs sampler is a well-known sampling method in MCMC, which can repeatedly draw samples from the conditional distribution of each variable.

The sampling process is shown below,

$l \leftarrow 1$
repeat
  $\mathbf{r}^{[l+1]} \leftarrow [\mathbf{r}|\gamma^{2,[l]}, \sigma_0^{2,[l]}, \mathbf{P}]$
  $\mathbf{q}_i^{[l+1]} \leftarrow [\mathbf{q}_i|\mathbf{r}^{[l+1]}, \gamma^{2,[l]}, \sigma_0^{2,[l]}, \mathbf{p}_i]$
  $\gamma^{2,[l+1]} \leftarrow [\gamma^2|\mathbf{Q}^{[l+1]}, \mathbf{r}^{[l+1]}, \mathbf{P}]$
  $\sigma_0^{2,[l+1]} \leftarrow [\sigma_0^2|\mathbf{Q}^{[l+1]}, \mathbf{r}^{[l+1]}, \mathbf{P}]$
  $\lambda^{2,[l+1]} \leftarrow [\lambda^2|\mathbf{r}^{[l+1]}]$
  $l \leftarrow l + 1$
until convergence

3.2 Posteriors

The operation of the Gibbs sampler requires the calculation of posterior PDFs. It can be shown that the posterior PDFs of $\mathbf{q}_i$, γ^2, λ^2 and σ_0^2 have the same form as the prior PDFs:

$$[\mathbf{q}_i|\mathbf{r}, \mathbf{p}_i, \text{rest}] \propto \mathcal{CN}(\mathbf{q}_i; \mu_q(\mathbf{r}), \mathbf{\Omega}_{sq}(\mathbf{r})), \tag{11}$$

$$[\gamma^2|\text{rest}] \propto \mathcal{IG}(a_\gamma^{\text{post}}, b_\gamma^{\text{post}}), \tag{12}$$

$$[\lambda^2|\text{rest}] \propto \mathcal{IG}(a_\lambda^{\text{post}}, b_\lambda^{\text{post}}), \tag{13}$$

and,

$$[\sigma_0^2|\mathbf{P}, \text{rest}] \propto \mathcal{IG}(a_{\sigma_0}^{\text{post}}, b_{\sigma_0}^{\text{post}}), \tag{14}$$

where $\mu_q(\mathbf{r})$ and $\mathbf{\Omega}_{sq}(\mathbf{r})$ denote the posterior mean and covariance matrix of the sonon amplitudes, while a_γ^{post},b_γ^{post}, $a_{\sigma_0}^{\text{post}}$, $b_{\sigma_0}^{\text{post}}$, a_λ^{post} and $b_\lambda^{\text{post}}$are the posterior shape and scale parameters of inverse Gamma PDFs.

For the posterior PDF of $\mathbf{r}$, some caution is needed. After some manipulation we get that $\mathbf{r}$ obeys the following distribution,

$$[\mathbf{r}|\mathbf{P}, \text{rest}] \propto \prod_{i=1}^{I} [\mathbf{r}]\mathcal{CN}(\mathbf{p}_i; 0, \mathbf{\Sigma}_p(\mathbf{r})). \tag{15}$$

where the covariance matrix $\mathbf{\Sigma}_p$ is function of $\mathbf{r}$. The latter has no closed-form solution, which leads us to resort to another numerical technique.

3.3 Hamiltonian Monte Carlo (HMC)

HMC is an MCMC sampling method for high-dimensional probability distributions. It merges the spirit of Hamiltonian dynamics and Monte Carlo sampling to produce an efficient sampling procedure [15, 16].

It basically extends the Gibbs sampler with the auxiliary variable

$$\mathbf{u} = \partial \mathbf{r}/\partial t, \tag{16}$$

which is considered as the speed of the sonons as they travel in space, through the iterations (time t) of the Gibbs sampler.

The aim of HMC is to draw in the auxiliary PDF $[\mathbf{u}|\mathbf{r}, \mathbf{P}, \text{rest}]$ instead of in the complicated posterior PDF $[\mathbf{r}|\mathbf{P}, \text{rest}]$. This process forms a joint PDF,

$$[\mathbf{r}, \mathbf{u}|\mathbf{P}, \text{rest}] = [\mathbf{u}|\mathbf{r}, \mathbf{P}, \text{rest}][\mathbf{r}|\mathbf{P}, \text{rest}], \tag{17}$$

which immediately returns the target PDF when marginalized over the speed $\mathbf{u}$. By analogy with Hamiltonian dynamics, the Hamiltonian reads,

$$\begin{aligned} H(\mathbf{r}, \mathbf{u}) &= -\log[\mathbf{u}|\mathbf{r}, \mathbf{P}, \text{rest}] - \log[\mathbf{r}|\mathbf{P}, \text{rest}] \\ &= K(\mathbf{r}, \mathbf{u}) + U(\mathbf{r}), \end{aligned} \tag{18}$$

where $K(\mathbf{r}, \mathbf{u})$ and $U(\mathbf{r})$ are the kinetic and the potential energies of the target PDF, respectively. By solving the Hamiltonian differential equation - Eqn. (20), we can achieve alternate sampling in the auxiliary and target PDFs.

A convenient choice for the distribution of the auxiliary variables $\mathbf{u}$ is the real Gaussian PDF, $\mathcal{N}(\mathbf{0}, \mathbf{I})$, which gives the kinetic energy,

$$K(\mathbf{r}, \mathbf{u}) = \mathbf{u}^H \mathbf{u}. \tag{19}$$

Therefore, the final HMC process to sample the posterior PDF $[\mathbf{r}|\mathbf{P}, \text{rest}]$ is,

1: $l \leftarrow 1$
2: **repeat**
3: $\quad \mathbf{u} \sim (\mathbf{0}, \mathbf{I})$.
4: $\quad$ Move the sonons in the phase space $(\mathbf{r}, \mathbf{u})$ to explore a new pair of parameters $(\mathbf{r}^*, \mathbf{u}^*)$ by,

$$\begin{cases} \frac{\partial \mathbf{r}}{\partial t} &= \frac{\partial H}{\partial \mathbf{u}} &= \mathbf{u}_n \\ \frac{\partial \mathbf{u}}{\partial t} &= -\frac{\partial H}{\partial \mathbf{r}} &= -\frac{\partial U}{\partial \mathbf{r}}. \end{cases} \tag{20}$$

5: $\quad$ Accept or reject the proposal $(\mathbf{r}_n^*, \mathbf{u}_n^*)$ based on the Metropolis-Hastings acceptance criterion [17, 18]

$$\alpha < \min\left(1, \exp(-H(\mathbf{r}_n^*, \mathbf{u}_n^*)) + H(\mathbf{r}_n, \mathbf{u}_n))\right), \tag{21}$$

$\quad$ where α is a random number drown from a uniform PDF $U(0, 1)$
6: $\quad l \leftarrow l + 1$
7: **until** convergence

It can be noticed from step 4 that the algorithm is making use of the gradient information of the target distribution, stored in the potential energy U, to generate the motion of the sonons; this exhibits another benefit of HMC, where gradient information enables Markov chains to converge quickly to the target distribution.

4. NUMERICAL DATA VALIDATION

The gridless method is assessed here using three different test cases. One is the identification of uncorrelated sources and the reconstruction of their directivity in 2D, and then similar aims are sought for correlated sources in 3D, the other analyzes the far field directivity of a trailing edge. In these test cases, the array configuration depends on the dimensionality of the problem, the characteristics of the source and the desired accuracy of the reconstructed field. The number of sonons used can simply be chosen from the number of peaks in the CBF map and can be increased to achieve a more precise correlation.

4.1 Two uncorrelated sources in 2D

The first test case simulates two point sources emitting uncorrelated white Gaussian signals with standard deviations 1 and 0.5, measured by a 60-microphone array (see Fig. 1). The two sources are located in the (x, y) plane at $(-0.1, 0)$ m and $(0.3, 0)$ m, while the array is placed at a distance $z = 0.1$ m from the source plane. The analysis frequency is $f = 1000$ Hz and the SNR is set to 20 dB to all the microphones.

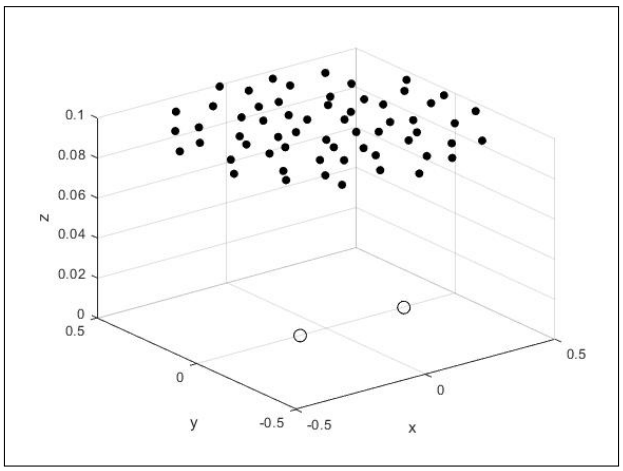

Figure 1. Configuration comprising two uncorrelated point sources and a 60 microphone array.

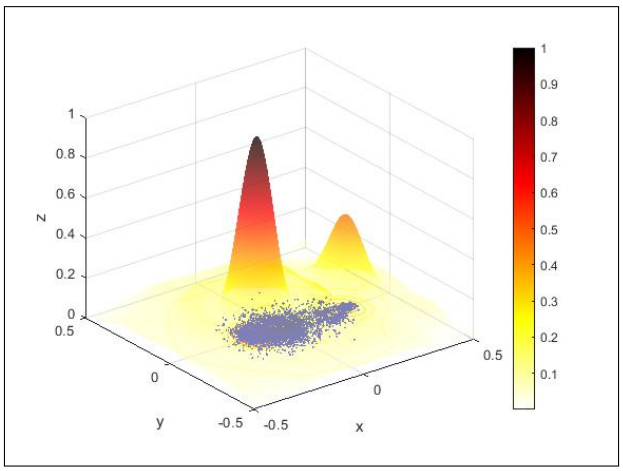

Figure 2. Absolute value of the normalized potential energy function $U(\mathbf{r}) = -\log[\mathbf{r}|\mathbf{P}, \text{rest}]$ with samples of the distribution $[\mathbf{r}|\mathbf{P}, \text{rest}]$ (blue points).

To set up the Gibbs sampler, the number of sonons used to reconstruct the original sound field is chosen as $N = 5$. Their starting positions are initialized by a uniform PDF in the region of interest. Other parameters are randomly initialized by their respective prior PDFs. The algorithm is run for 500 iterations.

Fig. 2 shows an example of a two-dimensional potential energy function $U(\mathbf{r})$ and the final sample cluster of 5 sonons samples. It can be observed that the samples adequately explore the high-probability region of the target distribution, where the real sources are located.

To see the behavior of the chain more clearly, Fig. 3 shows how the positions of the five sonons change with iterations. It can be noted that they fluctuate around the position of the real sources and occasionally cross modes, sampling from one potential energy region to another.

Eventually, the five sonons converge near the location of the real source and the energy of the original sound field is distributed to each of them. Since the phase and correlation information is stored in $\mathbf{q}$, we can observe how its reconstructed directivity compares to the directivity of the original sound field. (see Fig. 4). It is worth mentioning that the directivity is calculated in the (x, y) plane, at 1m from the origin and averaged over the last 50 iterations.

4.2 Two correlated sources in 3D

A similar analysis is tested in 3D, with source positions at $(-0.1, -0.1, -0.2)$ m, $(0.2, 0.1, 0.2)$ m and the array placed at $z = 0.5$ m from the xy plane. For this case, the source signals are two correlated Gaussian noises. For the Gibbs sampler setup, the number of sonons and the number of iterations are the same as in the 2D case.

Fig. 5 shows the Markov chains of the five sonons as they explore the posterior PDF. It can be seen that two sonons converge quickly to the locations of the true sources, while the other keep on exploring the 3D space with strengths close to 0.

Again, the directivity is reconstructed in the same way as in the 2D case, and we can clearly observe from Fig. 6 the consistency of the sound field generated by the sonons.

4.3 Trailing edge noise radiation

In order to test the capability of the method to reconstruct more intricate aeroacoustic sound fields, the case of the airfoil trailing edge noise is analyzed.

The analytical model for the theoretical sound field radiated by trailing edge noise is based on Amiet's model [19], the derivation of which can be found in [20]. It should be noted that only the first-order leading edge back-scattering correction has been considered. Fig. 7 shows the simplified airfoil configuration, where a circular array with $M = 200$ microphones is chosen in order to reconstruct the directivity pattern at the mid-span plane at a distance of 1m.

For the Gibbs sampler, the number of sonons is $N = 200$ and the algorithm is run for 200 iterations. The test is analyzed at two frequencies $f = 500$ Hz and $f = 1000$

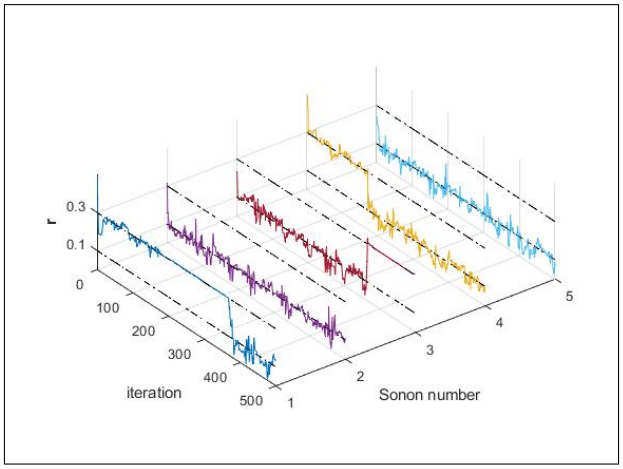

Figure 3. Markov chains of sonon positions $\mathbf{r}$. Different colors represent the chain for each sonon. The dashed lines represent the positions of real sources.

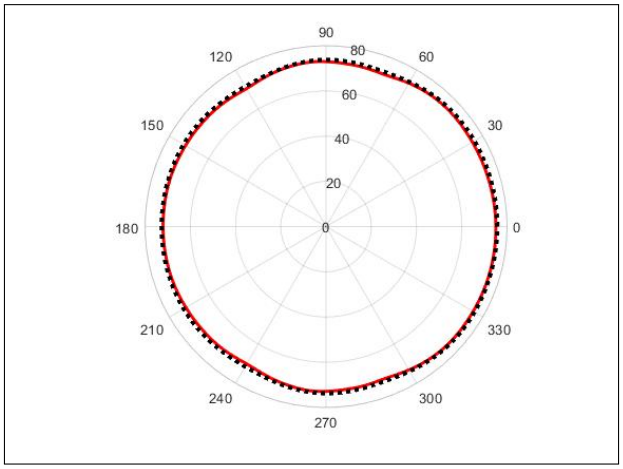

Figure 4. Directivity of the original sound field (black dashed curve) and of the 2D field reconstructed by the sonons (red curve) for the last 50 iterations averaged (dB scale).

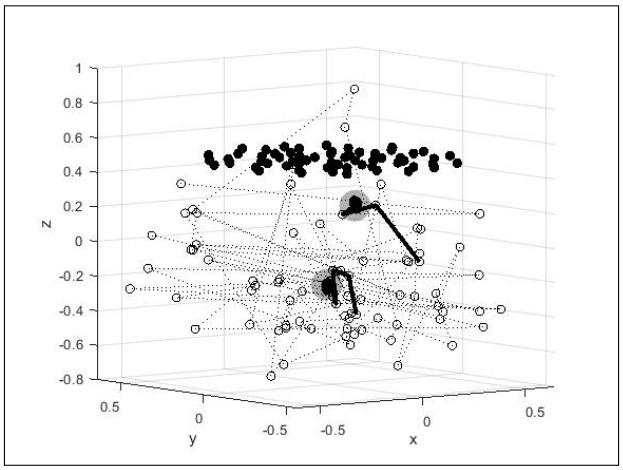

Figure 5. Markov chains of the sonon positions $\mathbf{r}$ in 3D space. The black solid points represent the microphone array. The grey points represent the real sources. The black lines are the converged chains and the black dashed lines are the chains still in exploration. The black hollow points are the chain samples.

Hz. The algorithm is launched in 3D and the directivity is reconstructed in the same way as before. The Mach number is 0.05 in the positive direction of the x-axis.

As can be seen in Fig. 8 and Fig. 9, the composition of 200 sonons is well able to reproduce the complicated trailing edge noise field. The latter exhibits the radiation characteristics of an acoustic dipole and, as the frequency increases, the pattern tends to deflect towards the leading edge and to show a cardioid shape. At 500Hz the sonons accurately reproduce the small fluctuations in the original directivity.

At 1000 Hz, with the same number of sonons, the directivity pattern is also mostly reconstructed. The principal dipole behavior as well as the main lobe deflected towards the leading edge are clearly seen. At higher frequencies, short oscillations appear in the directivity pattern, and these require an increased number of sonons to be accurately reconstructed.

In general, the results of the sound field reconstruction will be sufficient for the user to comprehend the main radiation characteristics, even if some spatial details cannot be fully captured with a limited number of sonons.

5. CONCLUSION

The results shown in the papar demonstrate the effectiveness of the new gridless method. It has major advantages.

First, the sampled sonons are free to move continuously in space and can accurately find the actual source locations without requiring a predefined grid.

Next, by recovering the phase and correlation information, a reconstruction of the directivity is achieved,

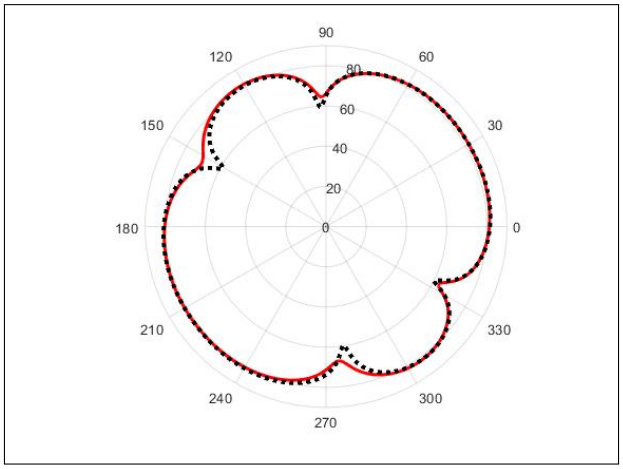

Figure 6. Directivity of the original sound field (black dashed curve) and of the 3D field reconstructed by the sonons (red curve) for the last 50 iterations averaged (dB scale).

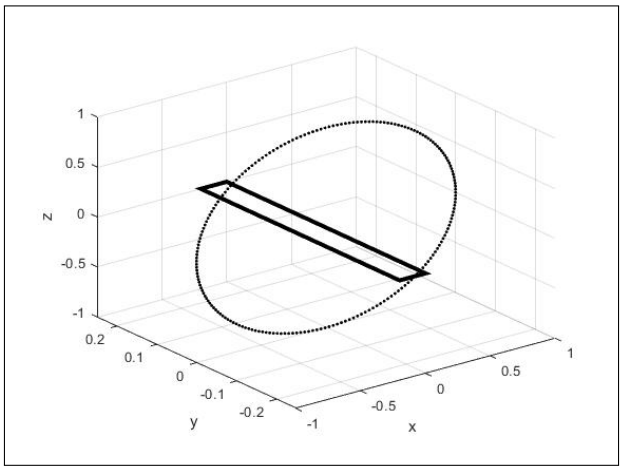

Figure 7. Configuration of the airfoil and of the 200 circular microphone array.

which provides unique insight into the sound field radiation properties.

The inclusion of a source position prior to the Bayesian framework in the three-dimensional gridless model also provides some flexibility, by allowing the incorporation of physical knowledge.

Of course, the correct tuning of the Hamiltonian Monte Carlo is necessary for implementing the gridless method. One perspective of future work will focus on automating the tuning of HMC. This will aim to minimize the discretization error in resolving the Hamiltonian equations.

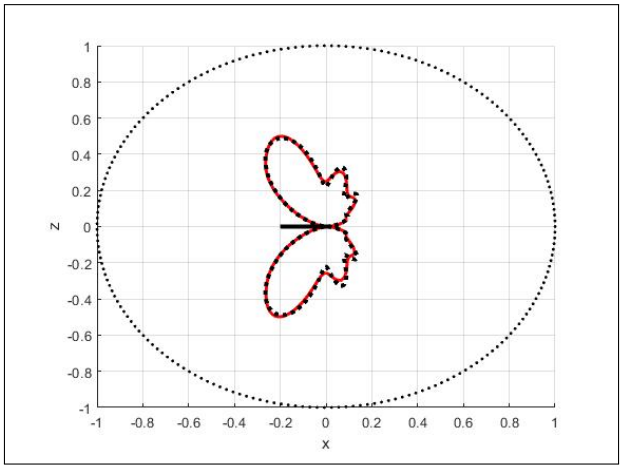

Figure 8. Directivity at 500Hz of the airfoil trailing edge at the mid-span plane: theoretical sound field (black dashed curve) and the 3D field reconstructed by the sonons (red curve) for the last 50 iterations averaged.

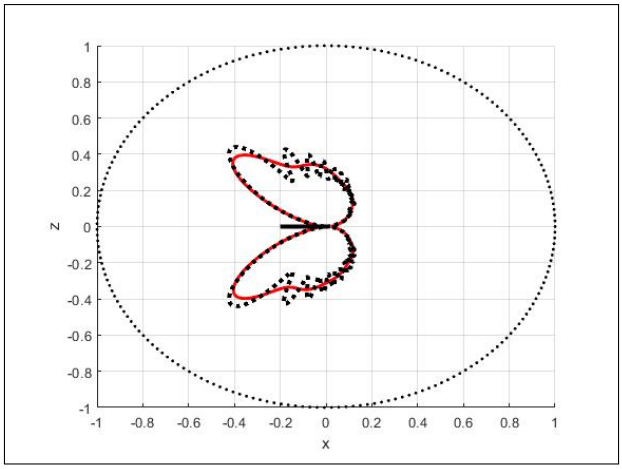

Figure 9. Directivity at 1000Hz of the airfoil trailing edge at the mid-span plane: theoretical sound field (black dashed curve) and the 3D field reconstructed by the sonons (red curve) for the last 50 iterations averaged.

6. REFERENCES

[1] P. Chiariotti, M. Martarelli, and P. Castellini, "Acoustic beamforming for noise source localization–reviews, methodology and applications," *Mechanical Systems and Signal Processing*, vol. 120, pp. 422–448, 2019.

[2] A. Xenaki and P. Gerstoft, "Grid-free compressive beamforming," *The Journal of the Acoustical Society of America*, vol. 137, no. 4, pp. 1923–1935, 2015.

[3] Y. Yang, Z. Chu, Z. Xu, and G. Ping, "Two-dimensional grid-free compressive beamforming," *The Journal of the Acoustical Society of America*, vol. 142, no. 2, pp. 618–629, 2017.

[4] G. Chardon and U. Boureau, "Gridless three-dimensional compressive beamforming with the sliding frank-wolfe algorithm," *The Journal of the Acoustical Society of America*, vol. 150, no. 4, pp. 3139–3148, 2021.

[5] A. M. Malgoezar, M. Snellen, R. Merino-Martinez, D. G. Simons, and P. Sijtsma, "On the use of global optimization methods for acoustic source mapping," *The Journal of the Acoustical Society of America*, vol. 141, no. 1, pp. 453–465, 2017.

[6] L. Wei, F. Ren, Z. Qin, B. Gao, Z. Zhang, J. Guo, C. Hou, and H. Li, "Acoustic sources imaging by partial swarm optimization in 3d," in *2021 4th International Conference on Information Communication and Signal Processing (ICICSP)*, pp. 284–288, IEEE, 2021.

[7] Q. Zhai, F. Ning, Z. Deng, H. Hou, J. Li, J. Wei, and B. Li, "A grid-free global optimization algorithm for sound sources localization in three-dimensional reverberant environments," *Mechanical Systems and Signal Processing*, vol. 188, p. 109999, 2023.

[8] Sarradj, "Three-dimensional gridless source mapping using a signal subspace approach," in *Proceedings on CD of the 9th Berlin Beamforming Conference, 8-9 June, 2022*, 2022.

[9] P. Castellini, N. Giulietti, N. Falcionelli, A. F. Dragoni, and P. Chiariotti, "A neural network based microphone array approach to grid-less noise source localization," *Applied Acoustics*, vol. 177, p. 107947, 2021.

[10] A. Kujawski, G. Herold, and E. Sarradj, "A deep learning method for grid-free localization and quantification of sound sources," *The Journal of the Acoustical Society of America*, vol. 146, no. 3, pp. EL225–EL231, 2019.

[11] J. M. Vera-Diaz, D. Pizarro, and J. Macias-Guarasa, "Towards end-to-end acoustic localization using deep learning: From audio signals to source position coordinates," *Sensors*, vol. 18, no. 10, p. 3418, 2018.

[12] J. Chambon, J. Antoni, and S. Bouley, "Galerkin equivalent sources method for sound field reconstruction around diffracting bodies," *The Journal of the Acoustical Society of America*, vol. 152, no. 4, pp. 2042–2053, 2022.

[13] J. Antoni, "A bayesian approach to sound source reconstruction: Optimal basis, regularization, and focusing," *The Journal of the Acoustical Society of America*, vol. 131, no. 4, pp. 2873–2890, 2012.

[14] J. Antoni, C. Vanwynsberghe, T. Le Magueresse, S. Bouley, and L. Gilquin, "Mapping uncertainties involved in sound source reconstruction with a cross-spectral-matrix-based gibbs sampler," *The Journal of the Acoustical Society of America*, vol. 146, no. 6, pp. 4947–4961, 2019.

[15] M. Betancourt, "A conceptual introduction to Hamiltonian Monte Carlo," *arXiv preprint arXiv:1701.02434*, 2017.

[16] R. M. Neal *et al.*, "MCMC using Hamiltonian dynamics," *Handbook of markov chain monte carlo*, vol. 2, no. 11, p. 2, 2011.

[17] N. Metropolis, A. W. Rosenbluth, M. N. Rosenbluth, A. H. Teller, and E. Teller, "Equation of state calculations by fast computing machines," *The journal of chemical physics*, vol. 21, no. 6, pp. 1087–1092, 1953.

[18] W. K. Hastings, "Monte carlo sampling methods using markov chains and their applications," 1970.

[19] R. K. Amiet, "Noise due to turbulent flow past a trailing edge," *Journal of sound and vibration*, vol. 47, no. 3, pp. 387–393, 1976.

[20] M. Roger and S. Moreau, "Back-scattering correction and further extensions of amiet's trailing-edge noise model. part 1: theory," *Journal of Sound and vibration*, vol. 286, no. 3, pp. 477–506, 2005.